Design and first operation of a supersonic gas jet based beam profile monitor

Vasilis Tzoganis,[1,2] Hao D. Zhang,[1,2,*] Adam Jeff,[1,2,3] and Carsten P. Welsch[1,2]
[1]*Cockcroft Institute, Warrington WA44AD, United Kingdom*
[2]*Physics Department, University of Liverpool, Liverpool L697ZE, United Kingdom*
[3]*CERN, 1211 Geneva, Switzerland*
(Received 14 November 2015; revised manuscript received 2 August 2016; published 12 June 2017)

Noninterceptive beam profile monitors are of great importance for many particle accelerators worldwide. Extra challenges are posed by high energy, high intensity machines and low energy low intensity accelerators. For these applications, existing diagnostics are no longer suitable due to the high power of the beam or the very low intensity. In addition, many other accelerators, from medical to industrial will benefit from a noninvasive, real time beam profile monitor. In this paper we present a new beam profile monitor with a novel design for the nozzle and skimmer configuration to generate a supersonic gas jet meeting ultrahigh vacuum conditions and we describe the first results for such a beam profile monitor at the Cockcroft Institute. This monitor is able to measure two-dimensional profiles of the particle beam while causing negligible disturbance to the beam or to the accelerator vacuum. The ultimate goal for this diagnostic is to provide a versatile and universal beam profile monitor suitable for measuring any beams.

DOI: 10.1103/PhysRevAccelBeams.20.062801

I. INTRODUCTION

Noninvasive or minimally invasive beam profile measurements which can operate in real time are desirable for any particle accelerators. Some of the possible hosts for such a device are the Large Hadron Collider (LHC) at CERN and its future upgrades, and the high power linac at the European Spallation Source (ESS) [1] where the power of the beam does not allow conventional diagnostics to operate. For low energy antiparticle storage rings such as the ultralow energy storage ring (USR) [2] and the extra low energy antiproton ring (ELENA) [3], it is better to have a new breed of diagnostics to avoid deterioration of the particle beam and preserve the vacuum, because producing antiparticles is expensive.

Previously, noninvasive gas-based beam profile monitors have been considered, including residual gas ionization profile monitors (IPM) [4–8] and beam induced fluorescence monitors (BIF) [6,9–11]. IPMs operate by using an external electric field to collect the ions or electrons produced by the interaction of the projectile beam with the residual gas in the vacuum chamber, while BIFs observe the images from the fluorescence light emitted after the excitation of the residual gas by the projectile beam. When IPMs are used to measure the beam profile of low current beams, ion detection is preferred rather than electron detection because the generated ions will have a much lower transverse velocity spread than the generated electrons, due to their mass difference. The image broadening from the transverse thermal spread can be minimized by applying a higher extraction voltage to reduce the collection time. However, for high beam intensity, the space charge field from the projectile beam is comparable to the IPM extraction electric field. In this situation, electron detection is used with an additional parallel dipole magnetic field. The field is used to guide the electrons, which spiral around the magnetic field lines until they reach the detector; in this way it mitigates the influence of the space charge of the projectile beam. To obtain beam profiles in both transverse planes, two IPM's oriented at right angles have been suggested [9], but the two beam profiles are not acquired at exactly the same location. Nevertheless, in a very low pressure environment, such a device is limited in both acquisition speed and resolution due to signal reduction. For BIF monitors, not only is the cross section lower, but also the induced photons are emitted at all angles and are detected by the camera into a solid angle of about 10^{-4}. This results in a lower signal than that of an IPM equipped with a microchannel plate detector (MCP) and an amplification of 5 to 6 orders of magnitude. Therefore, a local pressure bump about 10^{-5} mbar is normally desired in the detection region even with an intensified CCD or a modern electron-multiplying CCD [10]. Unfortunately this limits its application in an ultrahigh vacuum environment. A feasible solution to these limitations is to use a cold (<20 K) supersonic gas jet shaped into a thin curtain which allows for two-dimensional beam profile imaging [12] in the same way as an interceptive screen. Such a monitor could be seen as an enhanced IPM where additional gas injection improves the reaction rate and resolution, and reduces the acquisition time, even in an

*Corresponding author.
hao.zhang@cockcroft.ac.uk

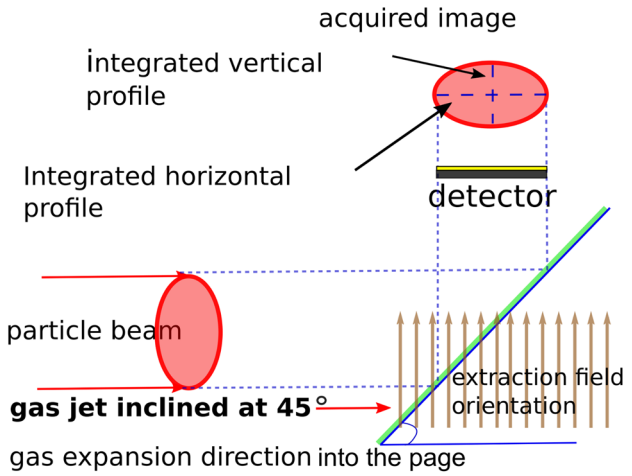

FIG. 1. Principle of two-dimensional imaging (ions are extracted by the external electric field).

ultrahigh vacuum environment. Furthermore it allows for a simultaneous determination of both transverse beam profiles in a single shot measurement by integration along the X or Y axis (see Fig. 1 for the two-dimensional imaging principle).

The use of gas jets in beam profile monitoring can be traced back more than four decades, when metal vapor [13,14] and carbon vapor [15] were used. Recently, it was applied in the Heavy Ion Medical Accelerator (HIMAC) [16] in Chiba, Japan, where an oxygen gas jet was used. This monitor [17] is skimmed and shaped to a thin curtain by focusing magnets [18] to measure the 2D profile of carbon ion beams. Another application by the same author was at the Japan Proton Accelerator Research Complex (J-PARC) [19]. With a molecular nitrogen jet it was possible to measure the proton beam bidimensional profile [20]. For both cases, the compression gauge or through gauge method was used to identify the 2D density distributions of the jets, which showed the thinness and homogeneity of the jet density distribution [17,21]. Another earlier example is a proton polarimeter with polarized atomic hydrogen jet, used as an independent beam profile monitor by Tsang *et al.* for the Relativistic Heavy Ion Collider (RHIC) at Brookhaven National Laboratory [22]. It uses the fluorescent light emitted by the excited hydrogen atoms from the interaction between the projectile proton beam and the hydrogen jet. As this monitor is not designed for the purpose, the beam profile measurement is limited to the vertical plane of the accelerator.

Compared to residual gas monitoring IPMs or fluorescence monitors, the supersonic gas jet based beam profile monitor offers several advantages. First, the monitor is intrinsically very flexible, in that the interaction it relies upon, namely ionization or fluorescence, is well understood and applicable to most projectile species. Second, operating parameters such as acquisition rate and beam perturbation can be easily scaled by varying the target gas density, and tailored for the particular application. The gas jet based beam profile monitor can therefore be used in most accelerators across large energy, current and vacuum ranges, and is not restricted only to low energy storage rings such as the USR, which is the target environment of our supersonic gas jet monitor. In the USR a low intensity antiproton beam with a short life time travels in an ultrahigh vacuum.

The basic components of the supersonic gas jet beam profile monitor closely match those needed for a reaction microscope (ReMi) which is a momentum spectroscope for analysis of fragmentation molecular and atomic reactions, as for example developed at the Max Planck Institute for Nuclear Physics in Heidelberg [23]. Currently, the supersonic gas jet monitor shares the design of components with the ReMi including the position sensitive detector for the imaging of ions, the electric field based extraction system and the supersonic gas jet target. Previously, it had also been proposed to operate the ReMi as a transverse beam profile monitor at the point of interaction [24].

The operating principle of gas jet beam profile monitor is as follows: At the particle beam-gas intersection point, ionization occurs and gas ions are created inside the collision volume. These ions are then extracted by an electric field of tunable strength provided by the extraction electrodes, and accelerated towards a position-sensitive detector composed of a MCP and a phosphor screen. The MCP can provide amplification of up to 10^6 without disturbing the position information on the phosphor screen. For every ion that enters the channels of the MCP a shower of electrons is produced, which impacts on the phosphor screen. As a result, visible light is produced and recorded by a camera located behind a transparent viewport outside the vacuum chamber.

In this paper, we describe in Sec. II the hardware design of the monitor and its experimental stand, and in Sec. III the working principle, including jet properties, ionization rate, and details of the monitor resolution, We discuss in Sec. IV the first operational experience with the pulsed valve and two different thicknesses of gas jet curtains, as used in an ultrahigh vacuum system to detect a low energy (~3.5 keV, ~7 μA) electron beam.

II. HARDWARE DESCRIPTION

A general description of the experimental setup is presented in Fig. 2. The gas is stored in a pressurized tank and released into the system with an initial pressure of 1–10 bars. As it travels downstream it passes through a 30 μm diameter circular nozzle which is laser drilled in a 300 μm thick platinum foil. At this stage, due to the high pressure difference ratio (~10^6 in our case), most of the collisions between the gas molecules occur in the high-density region near the nozzle. The gas molecules are accelerated by these collisions and undergo free expansion after the nozzle, resulting to the formation of a jet with a very cold inner core

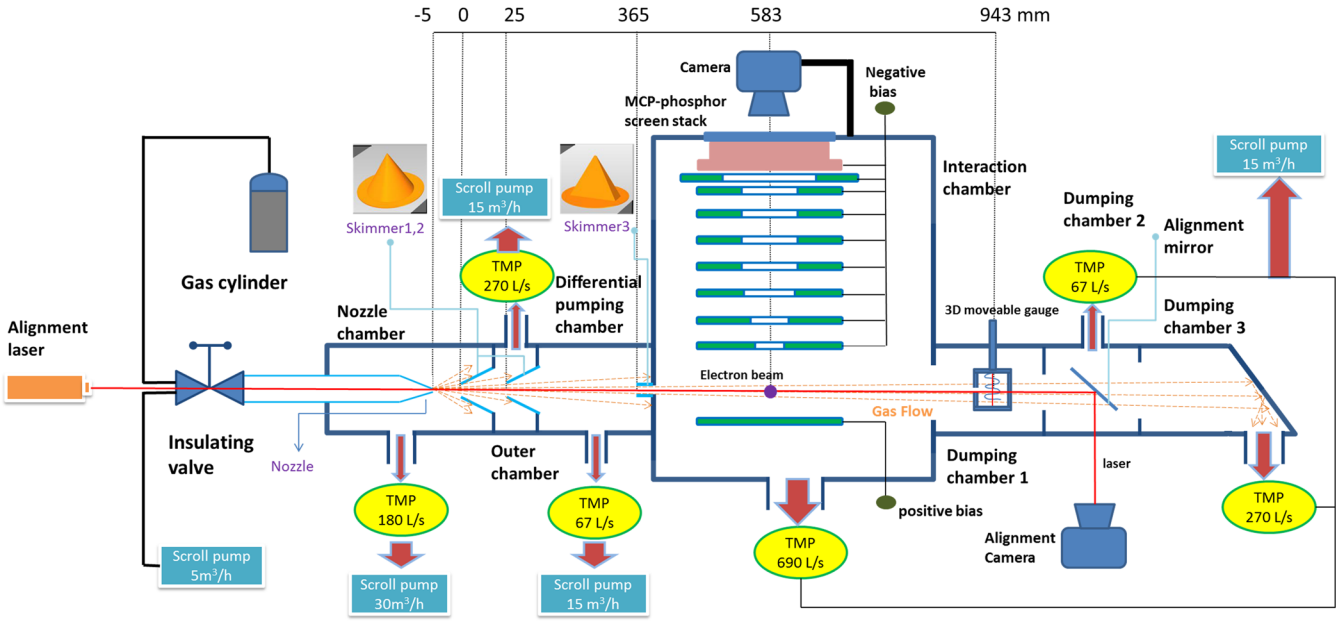

FIG. 2. General overview of the gas jet monitor setup (TMP: turbomolecular pump. The pumping speed is based on N_2 gas. TMPs for the outer and differential pumping chambers are backed by the same scroll pump).

stretching a few cm downstream from the nozzle [25]. Beyond that point the number of collisions decreases dramatically, until only a few collisions take place and the flow is said to be molecular, before any shock occurs. Given the nozzle size of 30 μm, the point beyond which no more collisions are expected to occur is in the order of a few mm from the nozzle. This is negligible compared to the distance to the interaction point, which is 583 mm.

To restrict gas usage and control gas flow, as well as to conserve better vacuum conditions, a MHE3-MS1H-3/2G-1/8 solenoid pulsed valve by Festo [26] is used. It features a maximum switching frequency of 280 Hz with 2 ms switching time, an operating pressure from 0 to 8 bar and a standard nominal flow rate of 200 l/ min. A TGP110 pulse generator manufactured by Aim & Thurlby Thandar Instruments [27] is used to trigger the pulsed valve externally. It offers a frequency range variable from 0.1 Hz to 10 MHz and an individually adjustable pulsed width and pulse delay. Its maximum output amplitude is 10 V, which is less than the required valve operating voltage of 24 V. A dc power supply IPS-3303 manufactured by ISO-Tech [28] and a solid state relay DMO063 manufactured by Crydom [29] are used to drive the valve. The electrical connection is shown is Fig. 3. The relay receives the 5 V trigger from the pulse generator and switches a 24 V signal to trigger the pulsed valve. An oscilloscope is used to monitor the generated pulse.

With reference to Fig. 2, the first skimmer is positioned less than 2 cm from the nozzle (indicated as 5 mm in the figure, but variable from 1 to 100 mm) to select only the inner part of the jet, which is highly directional and has a very low inner temperature of the order of a few Kelvin. The skimmer has a conical shape, and the diameter of the aperture is 180 μm. Most of the gas is pumped out between the nozzle and the first skimmer, and this results in less than 0.1% of the initially injected gas continuing to travel downstream. At a distance of 25 mm beyond the first skimmer, the second conical skimmer, of 400 μm diameter, skims the flow further. These two skimmers have been provided by Beam Dynamics Inc. [30], and are commonly used in gas jet generation experiments. They are manufactured from copper, with double wall thickness to withstand the large pressure differentials. They are named "model 7" where 7 is the nominal apex height, and have orifice diameters of 0.180 ± 0.025 and 0.400 ± 0.025 mm respectively, heights (from tip to base) of 6.6 and 6.2 mm, and a base diameter of 12.7 mm. The angle at the tip is 25°

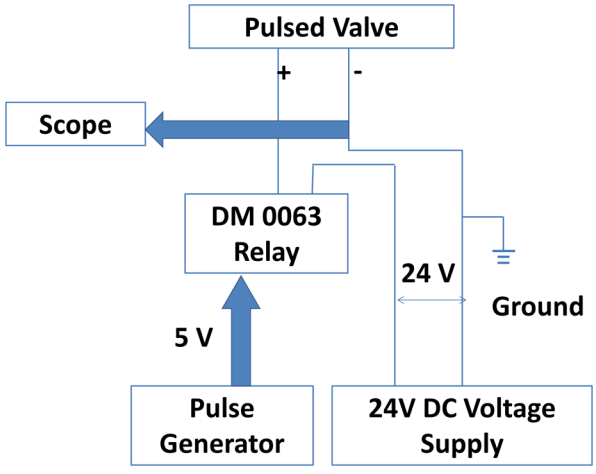

FIG. 3. Illustration of the pulsed valve operation and control.

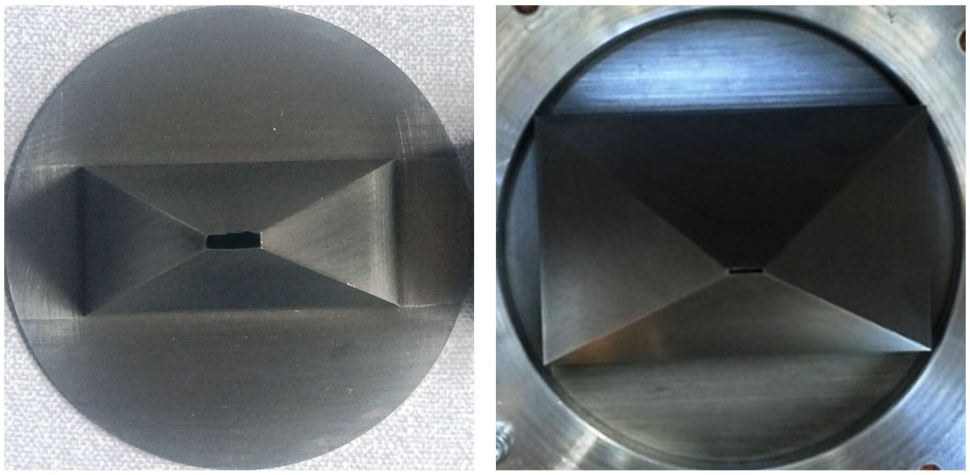

FIG. 4. Picture of the two different sizes of rectangular skimmer: (a) larger slit (7.2×1.8 mm^2); (b) smaller slit (4.0×0.4 mm^2).

internally and 30° externally, which becomes 75° at the base.

Two sizes are available for the rectangular-shaped skimmers, 7.2×1.8 mm^2 and 4×0.4 mm^2 as shown in Fig. 4, which are interchangeable and are placed 365 mm downstream of the first skimmer. They are normally rotated by 45° to create the thin tilted gas curtain. They were manufactured by Direct Metal Laser Sintering (DMLS), a laser-induced additive layering process usable on different metals including stainless steel. The skimmers have been constructed by the company CRDM UK Prototyping & Tooling and subsequently mechanically polished by TJW Precision, UK. This process guarantees very thin walls (100 μm) at the tip of the skimmer, comparable with the circular skimmer wall thickness. The set of three skimmers separates the vacuum chamber into differentially pumped volumes, to reduce the gas load and maintain an ultrahigh vacuum in the interaction area. After the final shaping, the jet enters the interaction chamber at the center of which, at a distance of 600 mm from the nozzle, it crosses the particle beam.

After the interaction, the remaining nonionized gas is evacuated by a turbomolecular pump (TMP) situated at the end of the vacuum duct, which faces the jet and is inclined at 45°. This angle is the same as that of the tilted blades of the turbo pump, thus maximizing evacuation efficiency under present conditions.

To operate such a monitor in a very high vacuum environment according to USR design parameters, which will reach 10^{-11} mbar pressure, strong differential pumping is required. Currently six TMPs are used, backed up by three prevacuum roughing pumps. One smaller roughing pump with a capacity of 5 m^3/h is used to evacuate the volume before the nozzle, for the case of pulsed operation of the gas jet. A detailed description of the experimental setup, including extensive discussion of the vacuum dynamics and the gas curtain formation, has been published elsewhere [31].

A. Detector and imaging

The detector assembly consists of a set of electrodes for the generation of the extraction field, a MCP paired with a phosphor screen, and a camera that sits outside the vacuum chamber. With reference to Fig. 5, the extraction system is composed of one repeller plate, nine ring electrodes (two of them to hold optional meshes) and the MCP detector assembly. The electrodes are supported by three metallic rods which are insulated from the plates by ceramic cylinders. The overall length of the system is 200 mm and the large gap between the repelling plate and the first electrode is 75 mm. The remaining rings are spaced at intervals of 16.5 mm, and the distances between the last electrode, the two optional meshes, and the bottom of the MCP are smaller. For voltage supply, two high voltage

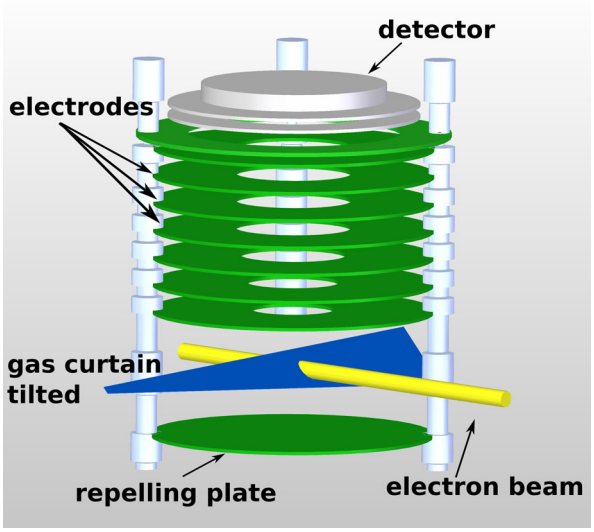

FIG. 5. Extraction field scheme and particle beam-gas jet interaction visualization.

power supplies from Microlab Devices [32] were used. They have two channels each, one for negative and one for positive voltage, and can provide up to ±6 kV. For the extraction electrodes, one negative channel is used, after passing through a voltage divider, to apply the proper voltage to every ring. The voltage is scaled according to the geometric distance between the electrodes, from −1800 V at the top to −400 V at the bottom, to generate a homogeneous electric field. The positive channel of the same power supply is used to bias the repelling plate at +400 V. The MCP and phosphor screen are connected to the positive and negative channels of the other power supply, biased at 3.5 and −2 kV, respectively. The voltage gradient is usually around 11 kV/m but can easily be adjusted to any value within the range of voltages which the power supplies can provide.

The main requirement for the extraction field is to extract the ions towards the MCP in a straight line, without deflecting the particle beam so much that it moves outside the gas curtain area or hits other elements in the experimental chamber. For a future version of the setup, compensating electrodes to apply corrective electric fields will also be considered.

The MCP detector is provided by Photonis [33]. It contains two plates stacked in a chevron configuration and a phosphor screen. The plates have a channel diameter of 10 μm and a pitch between channels of 12 μm, which are the parameters dominating the spatial resolution of the MCP. Including the effects of nonconstant amplification in the channel and electron smearing between plates, the actual resolution of this chevron type of MCP was reported by the manufacturer to be about 80 μm. The MCP can be biased up to 2.4 kV but it is usually kept lower than 2 kV for safer operation and improved longevity.

The phosphor screen used in this work is a common green-glowing P22 (ZnS:Cu,Al). It has a typical emission wavelength of 530 nm and a decay time of 70 μs. Such a long decay time may limit the acquisition speed of the monitor for pulsed beams. For the current experimental setup where a continuous beam is used, the decay time is not a concern. The camera is a Point Gray Grasshopper3 [34] 1920 × 1200 pixel CMOS camera with USB interface.

For calibration, a second phosphor screen at the end of a retractable arm can be moved to the center of the interaction region, providing direct imaging of the impinging particle beam.

B. Electron gun

For the development of the current setup, an electron gun was used to provide the projectile beam. It is a model ELS 5000 manufactured by PSP Vacuum Technology [35]. It has a common design for electron guns and provides a steerable electron beam with spot diameter <1 mm at the best focus, with energies from 1 to 5 keV and currents from 10 nA to 10 μA. It is mounted vertically to the propagation axis of the molecular beam, in one of the openings of the interaction chamber. The electron gun is usually operated nearly at the maximum kinetic energy and at a beam current allowing a clear signal to be seen on the camera. The filament current is usually between 2.0 and 2.6 A. The operating conditions of the electron gun must be adjusted every time the electric field configuration is changed, because the lack of correction fields causes the beam to bend under the extraction field forces. The electron beam current and intensity are selected to suit the extraction field strength and are then fine-tuned with respect to the image on the camera. The MCP and phosphor screen bias are also adjusted to obtain a clear image of the beam profile. It has been noted that when the filament current of the electron gun is above 2.3 A, there is a small pressure rise.

III. WORKING PRINCIPLE

The monitor presented here relies on a neutral, supersonic gas jet shaped into a thin curtain, which crosses the particle beam. As shown in Fig. 5, the gas screen flows perpendicularly to the propagation axis of the projectile beam, and the plane of the screen forms an angle of 45° with the particle beam axis.

The magnitude of the extraction electric field should be sufficient to extract the ions towards the detector, with only a small drift due to the initial ion velocity caused by the supersonic gas flow. After the intersection with the particle beam, the remainder of the gas jet is evacuated by flowing towards a dumping chamber, which prevents deterioration of the vacuum environment. The high directionality of the jet minimizes its influence on the overall low pressure conditions. Measurements proving the operating principle of this setup have been reported elsewhere [36].

In contrast to standard residual gas monitors, a curtain gas jet allows two-dimensional profile imaging of the transverse beam distribution, from which both of the one-dimensional beam profiles can be extracted by integration on separate axes.

A. Jet curtain properties

Figures 6(a) and 6(b) clearly describe the setup and the measurements, where the Z axis is along the direction of particle beam propagation, the X axis is along the gas jet propagation direction, and the Y axis is pointing upwards in the direction of the detector. The top view, which is the camera view of the system, shows how the above-mentioned coordinates corresponding to the measured beam profile coordinates. Ideally, ionization takes place at the center of the interaction area, but as the gas jet has an initial velocity, the imaged profile will be shifted along the X axis. This will provide a separation from the signal induced by residual gas. The particle beam horizontal and vertical profiles can be calculated by direct integration along the corresponding directions on the image acquired

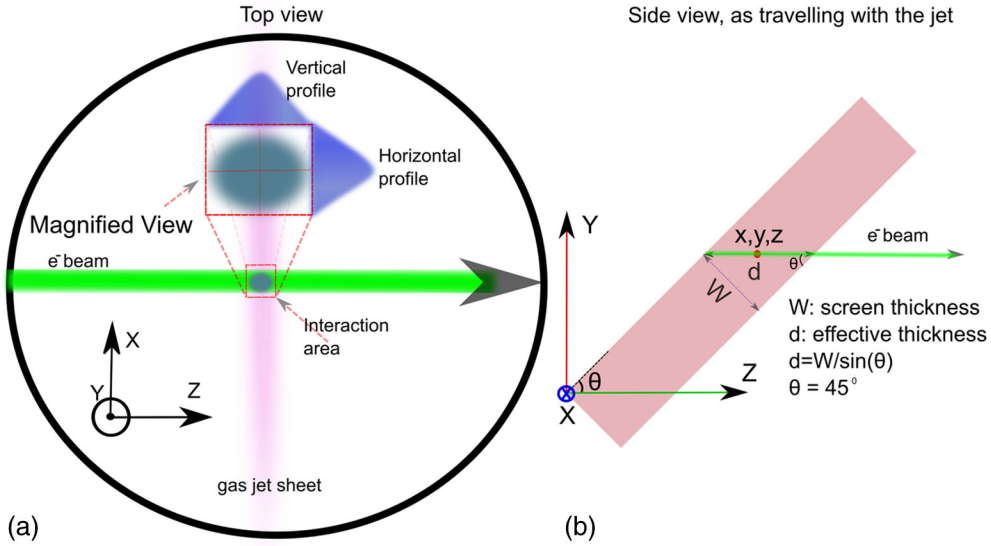

FIG. 6. (a) Schematic of the particle beam-gas jet interaction viewed from above. Gas jet sheet shown in purple, electron beam in green. (b) Side view and gas screen details.

by the camera. With reference to Fig. 6(b), for a jet curtain of thickness W, tilted at an angle θ of 45° with respect to the particle beam propagation axis (Z axis in the figure), the effective width, that is, the distance that the particle beam will travel in the jet d, is equal to $W/\sin(45°)$. In this case, a particle of the beam passing through the point (x, y, z) as noted in the figure, can ionize the gas anywhere in the segment $z \pm W/[2 \times \sin(45°)]$ along the Z axis. This adds an uncertainty to the measurement of the vertical beam profile, introducing an error that depends on the thickness W. In principle it is possible to minimize this error by increasing the angle, but the chosen value of 45° offers the advantage of maintaining the aspect ratio of the image profile, thus preventing any distortion which would require more complicated processing of the acquired images. The above-mentioned error contributes less to the measurement when the beam diameter is significantly larger than the jet thickness. The same issue has been reported elsewhere [17] and in this work special care was taken to create a thin gas curtain. The horizontal axis of the acquired profile is completely unaffected by the gas curtain thickness.

B. Acquisition time estimation

The acquisition time for our monitor depends on both the number of measurements required for a beam profile and the reaction rate. Statistically, for Gaussian beam diagnostics [37], accepting a confidence interval of 5% in beam position determination will require about 1500 ionization events to be recorded, which gives a 96% precision on the determination of the beam profile width [24]. The reaction rate R is given by

$$R = P_{\text{ion}} \cdot I/q_p, \tag{1}$$

where P_{ion} is the probability of ionization of a gas molecule by the projectile beam, I is the projectile flux in particles per second or projectile current, and q_p is the projectile charge. The probability can be expressed as

$$P_{\text{ion}} = \sigma_{\text{ion}} \cdot \rho_{\text{gas}} \cdot d_{\text{gas}}, \tag{2}$$

where σ_{ion} is the ionization cross section, ρ_{gas} is the gas target number density and d_{gas} is the gas curtain thickness. Ionization reaction rates for antiproton and electron impact will be discussed here. This is based on the electron beam available for the experimental setup and the antiproton beam of the USR.

For the case of the USR with antiprotons of 20–300 keV, a beam current of 1 nA, impacting on nitrogen or helium, with a typical gas jet density of 2.5×10^{16} particles/m^3 and a gas jet thickness of 0.5 mm, we calculate the expected reaction rates to be as shown in Fig. 7. The single ionization cross sections, for energies relevant to the USR beam and for helium and nitrogen, are available as measured with the ASACUSA slow antiproton beam line at CERN [38].

As shown in Fig. 7, the reaction rates are almost unchanged for the entire energy range of the USR. For helium this value is smaller than that of nitrogen due to its higher ionization energy. The acquisition time for a reasonable measurement of 1500 ionization events will be about 1 and 3 s for nitrogen and helium gas, respectively.

Nevertheless, the inherent flexibility of the device discussed here allows the reaction rates to be increased by simply increasing the gas pressure or using a larger nozzle. It should be noted however that any changes must be carefully considered, as they can affect the efficiency in the first stages of the differential pumping. Generally, particle densities of 10^{17} to 10^{18} m^{-3} are achievable [23].

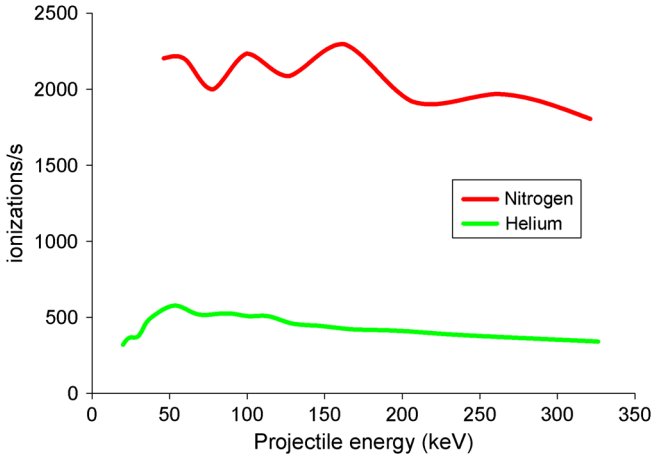

FIG. 7. Calculated reaction rates for antiprotons [38].

Regarding the experimental stand at the Cockcroft Institute, an electron beam with about 7 μA of beam current and a maximum energy 5 keV can be produced by the electron gun, for 2.5 A of filament current. Reaction rates are calculated using available data for electron impact ionization on various targets [39], with a number density of the gas jet of 2.5×10^{16} particles/m^3 and a gas jet thickness of 0.5 mm. The actual gases used are helium, nitrogen and argon.

As shown in Fig. 8, the reaction rate is much higher for electrons than that of antiprotons shown in Fig. 7 due to the higher beam current. For a typical value of 1.5×10^6 ionization events per second using nitrogen gas, the estimated acquisition time to obtain a meaningful measurement is about 1 ms. It should be noted that for argon, which is a heavier gas, the reaction rate is higher but the increased mass has detrimental effects on the instrument resolution. The internal momentum spread of the jet particles is critical for imaging resolution, and it scales with the mass m of the gas atoms as $\Delta P_{\text{jet}} \propto \sqrt{m}$ [23].

It should be stated that although the larger cross section of low energy beam particles favors the monitor, at the same time it limits the beam lifetime. Due to the higher reaction rate of the high density gas jet, part of the beam is lost at every pass. Cumulative losses after multiple passes, mainly applying to storage rings, reduce the beam lifetime. Based on this, the thickness and density of the jet can be fitted to the specific application, so that the signal intensity is sufficient while the particle beam is not disturbed.

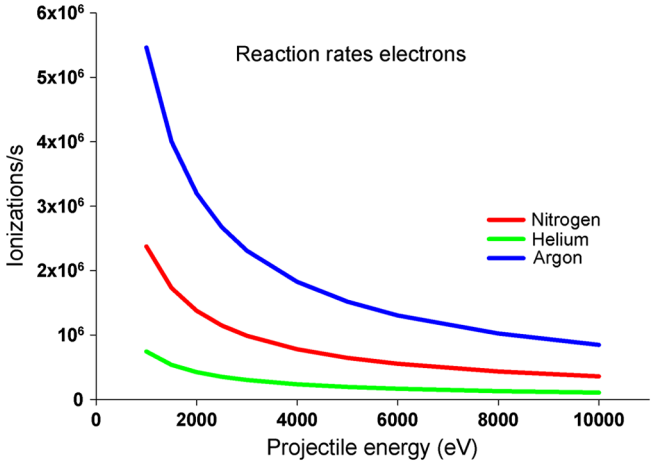

FIG. 8. Calculated reaction rates for electrons [39].

For the diagnostics of the USR beam, a residual gas pressure in the order of 10^{-11} mbar, corresponding to number densities at room temperature of about 10^{11} particles m^{-3}, would give a jet to residual gas density ratio of about 10^5. The effect of a 0.5 mm gas jet screen would equate to 50 m of residual gas, which is comparable to the storage ring circumference of 42.6 m. The beam lifetime therefore is expected to be roughly halved under the specified operating conditions.

C. Monitor resolution

Six main components define the final resolution of the monitor: these are camera resolution; MCP resolution; image broadening due to the gas jet curtain thickness; thermal velocity spread-induced image broadening; distortion caused by the space charge of the projectile beam; and a nonlinear external field.

Of these, the camera resolution σ_{CCD} can be easily improved with a high resolution camera and a lens suitable for the geometry of the detector. The MCP resolution is defined by the channel pitch, which is difficult and costly to change. The MCP is usually selected at the beginning of the detector design. As discussed previously, the resolution contribution from the MCP is $\sigma_{\text{MCP}} = 80$ μm in our case. The next component is the thickness of the gas jet. The jet acts as a thick screen and ionization can occur anywhere in the common volume of the particle beam and gas jet intersection. As shown in Fig. 6, for a screen with effective thickness d, the point spread function is stretched by a factor of d, which limits the resolution in the axis perpendicular to the direction of travel of the jet or the vertical beam profile. However, the resolution along the other axis is not affected.

The image broadening due to the jet thickness can be regarded as an error term added to the vertical beam size in quadrature. To quantify the jet thickness, a movable ionization gauge system was introduced to probe the gas jet density distribution [40]. As it comes out of the rectangular skimmer, the gas jet is assumed to be uniform and to have the same shape as the skimmer, which is 4.0 mm $\times$ 0.4 mm and is tilted by 32 degrees. Since most of the terms we use later are quoted as rms values, we can transform the uniform jet length and width (length is the large dimension of the jet and width the short one) to rms sizes of 1.2 mm $\times$ 0.12 mm using a conversion factor of $2\sqrt{3}$. The scanning gauge is located 578 mm downstream of the third skimmer (see Fig. 2), and thus cannot measure the gas jet density exactly at the interaction point of the

experimental chamber, which is 218 mm beyond the third skimmer. A vertical scan of the gas jet (1D measurement) showed that the gas jet has a Gaussian profile with a standard deviation of 1.0 mm [40]. Assuming the same aspect ratio and tilt angle as in the propagation process of the jet curtain, the rms size of the jet can be calculated as 1.9 mm × 0.19 mm at the position of the scanning gauge. The rms size of the jet can then be estimated as 1.5 mm × 0.15 mm at the interaction point when linear expansion is applied. Thus for the smaller third skimmer case, the image broadening from gas jet thickness will be $\sigma_{\text{jet}} = 0.15\ \text{mm}/\sin(32°) = 0.28$ mm, which will be taken into account by subtraction in quadrature. Similarly, with the same expansion rate, this broadening can be estimated for the larger third skimmer case (with size of 7.2 mm × 1.8 mm and tilt of 45 degrees), as $\sigma_{\text{jet}} = 0.91$ mm. Both the available rectangular skimmers are usually rotated by 45° to produce the tilted gas curtain. During the experiments mentioned here, only the small skimmer was positioned at 32°.

To determine the image broadening by thermal velocity spread and distortion due to the external electric field, we simulated the ion collecting process and examined how the expected beam profile is affected, using the PIC code WARP [41]. Initially, a round Gaussian N_2^+ beam with 10^6 particles was created at the interaction point. We assumed that the N_2^+ ion had the same velocity spread as a N_2 gas jet with a temperature of 10 K. The voltages for the repeller plate, top metallic ring electrode and MCP were 200, −1500 and −2200 V, respectively, which are similar to our normal experimental settings. The initial rms beam size was assumed to be 0.50 mm. In Fig. 9, we plot the potential of

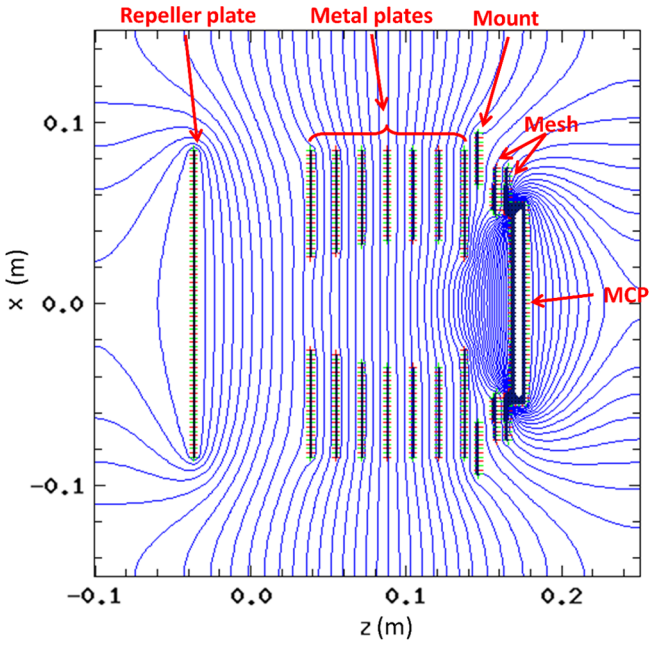

FIG. 9. Electrostatic potential in the z-x plane for the external ion-extraction field.

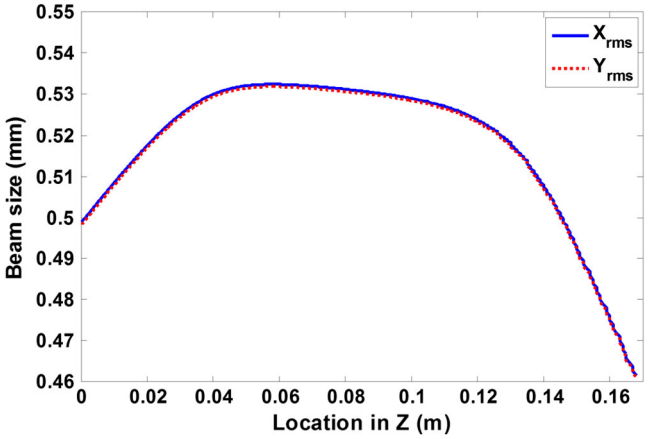

FIG. 10. The change in the ion beam size during propagation to the MCP under an external field.

the external electric field. The equipotential lines near the MCP are dense and curved, which indicates a large electric field in the z direction as well as a radial component. Figure 10 shows how the beam profile size changes during the drift process. Compared with Fig. 9, the radial component of the external field between the repeller plate and the first metal plate is insignificant because of the geometry of the current setup; in this case thermal spread will dominate the drift process. Thus, as indicated in Fig. 10, the slope of the beam size growth is quite large between z = 0.00 and 0.04 m. After the entry to the metal rings region between z = 0.04 and 0.12 m, the focusing field is moderate and reduces the beam size, countering the thermal velocity spread. Therefore, the growth of the beam profile size slows down and later decreases slightly. In the area between the last metal ring and the MCP, the radial component of the field is large enough to provide focusing to exceed the thermal spread, because of the rapid growth of the electric potential. As a result, the beam size shrinks. The final size of the beam is decreased to 0.46 mm, which is a combined effect from the thermal spread and the external focusing field.

To investigate this further, we scanned the initial rms N_2^+ ion beam size from 0.2 to 1.7 mm, keeping the total number of the simulated particles the same. The result for the expected beam size is shown in Fig. 11. Since the external field is radially symmetric, the external focusing field will magnify or demagnify the real beam size. In this sense, we can fit the data with the following formula:

$$\sigma_{\text{measured}} = \sqrt{M^2 \cdot {\sigma_{\text{real}}}^2 + {\sigma_{\text{thermal}}}^2}, \tag{3}$$

where M represents the magnification factor of the external field without consideration of the thermal spread and space charge effects; σ_{thermal} is the contribution from thermal spread. The curve fitted to this formula and also shown in Fig. 11 gives a magnification factor $M = 0.87$ and

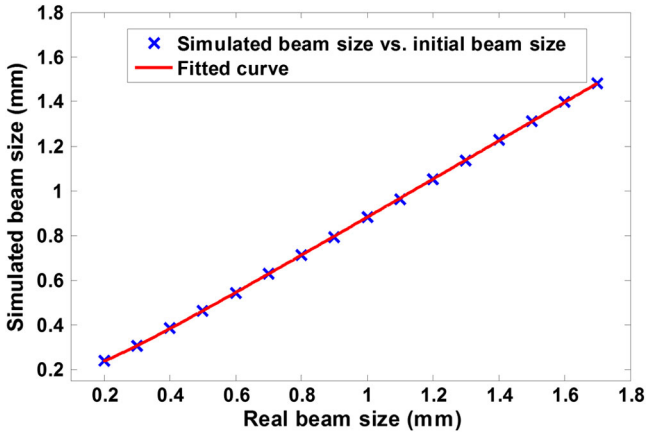

FIG. 11. Image broadening by thermal spread and radial component of the external field, with different initial or real beam sizes. The curve is fitted according to Eq. (1), with $R^2 = 1$.

$\sigma_{\text{thermal}} = 0.17$ mm. The R^2 value is 1.0, which indicates that the model is in perfect agreement with the simulation data. It should be noted that the magnification factor M is based on the particular external field settings, while the thermal spread depends on the drift time and ultimately on the external field setting in our case. Another test with voltages on the repeller plate, top metallic ring electrode and MCP of 300, −1300 and −2100 V, respectively, gives $M = 0.97$ and $\sigma_{\text{thermal}} = 0.17$ mm.

The final factor affecting resolution is the space-charge induced image distortion σ_{sc}. For our test stand, the current of the projectile electron beam is as small as a few microamperes, so that the induced space charge field is rather low compared with the external field and its distorting effect can therefore be ignored. There are however other applications of this monitor for which the space charge would be a key factor to consider for resolution, especially if it is used to detect the profile of a higher current beam. For the collection process, the distribution of the generated ions or electrons will be stretched in the X axis by the transverse space charge of the projectile beam. For the Y axis, the beam profile will be distorted by the longitudinal space charge or wakefield, if the projectile beam is pulsed. As in the IPM [42], a parallel dipole magnetic field could be applied and electrons will be detected. The broadening σ_{sc} will then be regarded as the spiralling radius, which depends on the guiding magnetic field and the initial velocities of the dissociated electrons. The latter can be estimated as an inelastic collision process [23] or determined experimentally [43]. In this case, the required magnetic dipole field must be unrealistically large for a reasonable resolution to be achieved, if ions are used.

Including all the effects contributing to the resolution in our case, the measured beam size may be represented as

$$\sigma_{\text{measured}} = \sqrt{M^2(\sigma_{\text{real}}{}^2 + \sigma_{\text{jet}}{}^2) + \sigma_{\text{thermal}}{}^2 + \sigma_{\text{sc}}{}^2 + \sigma_{\text{MCP}}{}^2 + \sigma_{\text{CCD}}{}^2}. \quad (4)$$

Table 1 summarizes each broadening term for our experiment: σ_{jet} applies only to the Y axis.

IV. MEASUREMENTS

This section has two parts, covering the operation of the jet with a pulsed valve and the presentation of profile measurements.

A. Gas jet working in pulsed mode

The gas jet can operate in pulsed mode to reduce the gas load on the vacuum system, minimize gas consumption and synchonize with the beam arrival to increase the signal to noise ratio. Figure 12 shows typical pressure curves for different chambers in pulsed mode operation, where the blue curve represents the valve operation. In this measurement, helium gas was used with an inlet pressure of six bars, and the valve was activated by pulses of 0.8 s period and 50% duty cycle. To measure the pressure of the differential and dump chambers, two Bayard-Alpert type ion gauges powered by an ion-gauge controller (IONIVAC IM 540) were used. The signals from the ion gauges (usually in nanoamperes) were collected and converted to voltages by two picoammeters and then recorded by the oscilloscope. When the pulsed valve is open, the pressures rise in both the differential and the dump chamber as shown in purple and red in Fig. 12. After the pulsed valve closes, the pressures drop, slowly approaching the base level. It should be noted that the pressure data has been smoothed using a moving average of the neighboring 20 points, which gives a time resolution of 8 ms. In a later analysis we vary the trigger period, duty cycle or inlet gas pressure as shown in Figs. 12 to 15, and the maximum and minimum pressures for the differential and dump chambers are

TABLE I. Summary of the image broadening terms for the experiment.

Error term	Value
σ_{jet}	0.28 mm
σ_{thermal}	0.17 mm
σ_{sc}	0
σ_{MCP}	0.08 mm
σ_{CCD}	0.08 mm

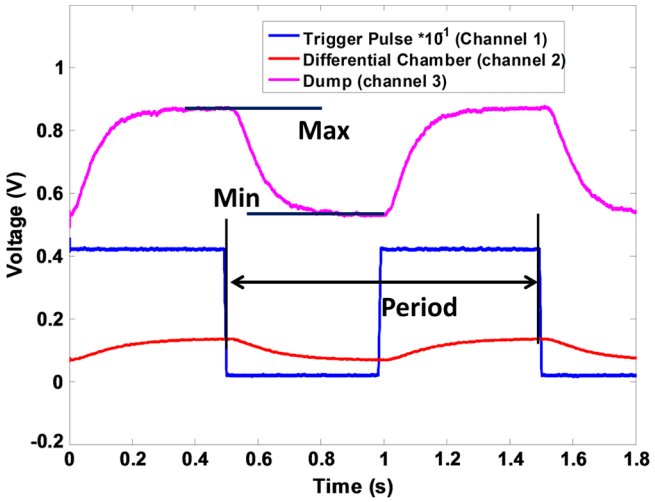

FIG. 12. Time structure of the pulsed valve and pressure response in the two chambers. The conversion factors between the displayed voltage (V) and the pressure in the chamber are 4.33×10^{-10} mbar/V for the differential chamber and 1.00×10^{-9} mbar/V for the dump chamber.

defined as the maximum and minimum of the corresponding curves, indicated as Max and Min in Fig. 12.

The parameters for the first experiment were (i) inlet pressure 2 bar; (ii) pulse duty cycle 50%; and (iii) pulse period from 0.1 to 2 s. Figure 13 suggests that with high-frequency pulses (short period), the pressures in both chambers reach a state in which the minimum and maximum values approach each other. With a longer period, the maximum and minimum pressures are more clearly discriminated, while the system has the time required to return to a higher vacuum by removing the injected gas. The transition period between the maximum and minimum pressures is about 0.8–0.9 s.

The parameters for the second experiment were (i) inlet pressure 2 bar; (ii) pulse duty cycle from 10% to 100%; (iii) pulse period 1 s.

The maximum and minimum pressures in both chambers are shown in Fig. 14. For a short duty cycle, the valve ON time is less than the OFF time, so the chamber has enough time to return to the base pressure, indicated by the minimum pressure staying constant for the short duty cycle. However, as the duty cycle increases, more gas is loaded into the chambers and the maximum pressure continues to grow within a single period. There is a transition in the duty cycle where the vacuum cannot return to the initial condition, which is about 40%–60%, corresponding to a 0.4–0.6 s period. Based on these results the differential and dump chambers will reach their highest possible background pressure for 2 bar inlet pressure, when the valve is enabled for about half a second; it requires about the same time to return to base pressure, which is considered the pressure before the gas jet operates.

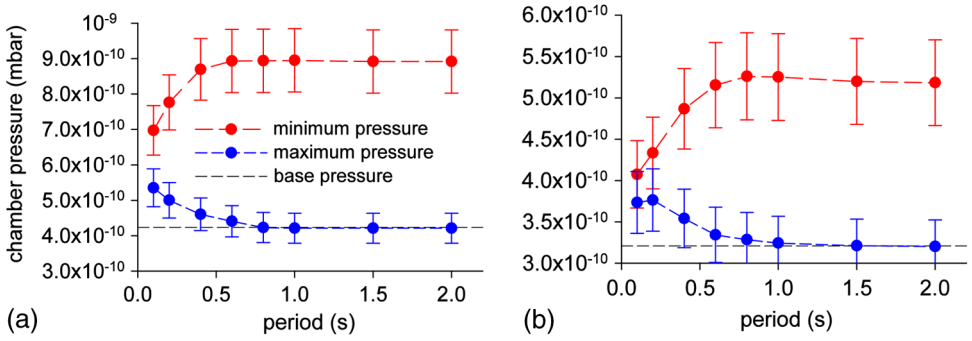

FIG. 13. Plot of pressure at (a) differential chamber and (b) dump chamber versus pulse valve period; the duty cycle of the pulsed valve is 50%, the pressure at the pulsed valve is 2 bar, and helium is the gas used.

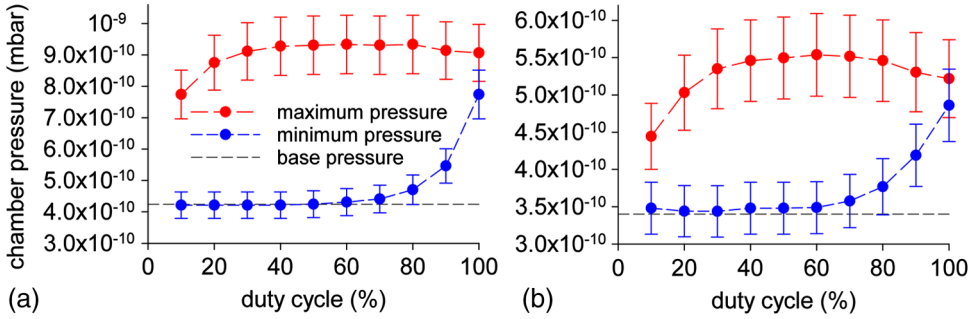

FIG. 14. Plot of pressure at (a) differential chamber and (b) dump chamber verses pulsed valve duty cycle; the period of the pulsed valve is 1 s, pressure at the pulsed valve is 2 bar and helium is the gas used.

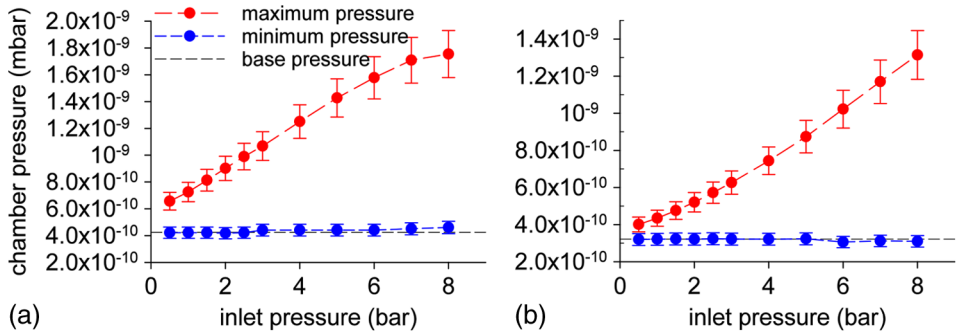

FIG. 15. Plot of pressure at (a) differential chamber and (b) dump chamber, versus inlet pressure, for 1 s period, 50% duty cycle, variable helium pressure.

The parameters of the third experiment were (i) inlet pressure variable; (ii) duty cycle 50%; (iii) pulse period 1 s.

As shown in Fig. 15, the maximum pressure in both chambers is linearly proportional to the inlet pressure. Meanwhile, the valve OFF time is sufficient for the pressure to return to the base level, which means that the minimum value for each case remains approximately constant in both chambers.

These results show a characteristic time of about half a second for the pressure to be restored to the base value after each cycle of the gas jet. The maximum pressures inside both the differential and the dump chambers scale reasonably linearly with the inlet gas pressure. They also suggest that by synchronizing the camera with the pulse and setting a proper shutter time, the ratio between the supersonic gas jet and the residual gas signals can at least be doubled.

B. Profile measurements

During the measurements presented in the first part of the following, the stagnation pressure (inlet gas pressure) was 5 bar, and the filament current and electron gun voltage were set between 2.40 and 2.60 A, and 3.5 and 4.0 kV, respectively. The electron beam intensity is controlled by the filament current; higher current increases the filament temperature which is the main contributor to electron emissivity. For the current setup, the electron beam in the interaction chamber will travel only 400 mm until it reaches the flange in the other side of the chamber. Reflected electrons or secondaries from this beam will travel back to the interaction area, interact with the residual gas and create a flat background noise. For this reason, the filament current is usually kept at the moderate value mentioned above, to obtain a better signal to noise ratio. In an actual beam line with a longer beam pipe. there will be no objects to stop or reflect the electron beam in the vicinity of the interaction area, and this noise will be negligible. Another parameter taken into account only for the experimental test stand is the deflection of the projectile electron beam from the e-gun by the external field. The deflection angle depends on the electron energy and the electric field between the repeller plate and the bottom ring electrode. To let the electron beam collide with the gas jet, we need to change the dipole setting of the gun, and the voltages of the metallic plate and the bottom ring electrode, as well as the electron energy. By adjusting these four parameters, we can also reduce some of the electron reflection into the metallic electrodes region, and thus decrease the background noise. The voltage applied to the MCP can be allowed to remain at a higher value, unless the image is saturated. The camera was mounted at about 11 cm distance from the top viewport.

1. *Large skimmer* (7.2×1.8 mm^2)

The image shown in Fig. 16(a) was acquired with the larger third skimmer (7.2×1.8 mm^2) installed. The voltage settings for the repeller plate, top metallic ring electrode, MCP and phosphor screen were 200, −1500, −2200, and 3000 V, respectively. The electric field gradient between the repeller plate and the bottom ring electrode was about 7.5 kV/m, as calculated from the simulation. The electron gun settings were 2.40 A for filament current and 3.75 keV for electron energy. Nitrogen gas was used in this experiment. The residual gas induced signal (the elongated line across the x axis) is also visible in the figure due to the high surrounding pressure of about 10^{-8} mbar. The separation between the gas jet and the residual gas induced signals is a result of the high initial velocity of the gas jet, as expected.

For the calibration of the image, the dimension of the phosphor screen on top of the MCP, which is known to be 75.0 mm, was used. This length translates to 900 pixels in the image and gives a calibration factor of 12.0 pixels/mm. If the camera were to be moved or repositioned at a different location, the calibration would need to be performed again. A region of interest (ROI) was chosen, as indicated with the dotted black line in Fig. 16(a), for the data analysis. Figure 16(b) shows the x projection of the ROI, and the fitted curve is the sum of two different Gaussian functions plus a constant. This constant is required to account for the background. Similarly, Fig. 16(c) shows the Y projection of the ROI, but here only one Gaussian function is fitted plus a constant. The fitting of the projected profiles gives a spot size of

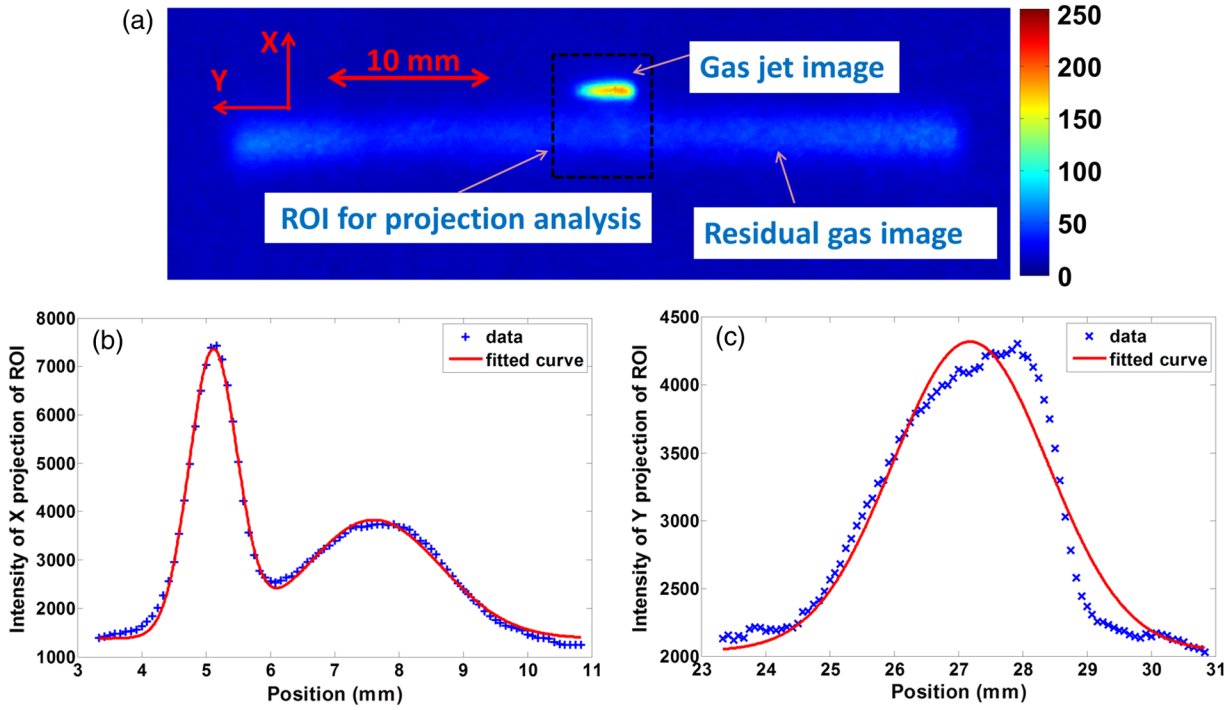

FIG. 16. (a) Images of electron beam measured from both the gas jet (larger size third skimmer) and residual gas; projected profiles in (b) x direction and (c) y direction (electron beam energy is 3.75 keV, external collecting E-field is 7.5 kV/m, the gas pulse duration time is 1 s and the exposure time of the camera is 70 ms).

$\sigma_{x\_\mathrm{jet}} = 0.37 \pm 0.01$ mm, $\sigma_{y\_\mathrm{jet}} = 1.21 \pm 0.09$ mm for the gas jet image and $\sigma_{x\_\mathrm{res}} = 1.05 \pm 0.05$ mm for the residual gas image. The error quoted here is the statistical error of the fit with a 95% confidence bound. From Eq. (1), the real X axis size will be $\sigma_{x\_\mathrm{real}} = 0.38$ mm. For the measurement of the residual gas image, the uncertainty from thermal spread will be much larger, as the temperature of the residual gas (room temperature) is about 30 times that of the gas jet. The generated ions from the residual gas-particle beam interaction have a much higher initial velocity spread than from the gas jet, which will cause a larger image broadening.

Note that the discrimination level between the background noise and the actual beam profile can also be determined using the average value of the darker area around the beam image. This value can change depending on the operating conditions, especially on the MCP gain, phosphor screen bias, and camera exposure time and gain. If the effect of the ion drift is subtracted from the beam size measurement with the supersonic gas jet, the other contributions to the resolution of the monitor in the current state can be evaluated as about 100 μm in the X axis. The measurement resolution in the X axis will be improved with a new camera and a lens with a field of view matched for the application. The position and mounting of the camera are also of high importance as they can introduce measurement errors.

In the Y axis, an additional error source is the thickness of the jet. As discussed above, we estimated this effect to be $\sigma_{\mathrm{jet}} = 0.91$ mm. Here we will use Eq. (2) to deduct both the thermal spread and the jet thickness, but we ignore the effect from the space charge and CCD and MCP smearing, resulting in a beam size of $\sigma_{y\_\mathrm{real}} = 1.03$ mm. As the size of the electron beam in both axes is almost the same, as seen at the rear phosphor screen which is 200 mm away from the interation point, and as there is no other field to deform the electron beam, the only obvious reason for the difference between σ_{y_real} and σ_{x_real} is that we underestimated the jet thickness. In reality, the jet might well not be homogenous and isotropic, on a larger scale.

2. *Small skimmer* ($4\times0.4\,\mathrm{mm}^2$)

By using the smaller third skimmer (4×0.4 mm2) the resolution in the Y axis was expected to be improved by producing a thinner gas curtain. The skimmer orientation angle was 32°. The nominal thickness of the gas curtain at the exit of the skimmer with this setup would be $0.4/\sin(32°) = 0.75$ mm, which is much smaller than previously $1.8/\sin(45°) = 2.55$ mm. After changing the third skimmer to the smaller one, the electron beam was slightly retuned and thus the results cannot be directly compared to the previous measurement. In order to compensate for the reduced brightness which is a result of the smaller ion production from the thinner gas curtain, the electron gun was set at 2.6 A filament current and 3.5 keV electron beam energy. The voltage settings for the

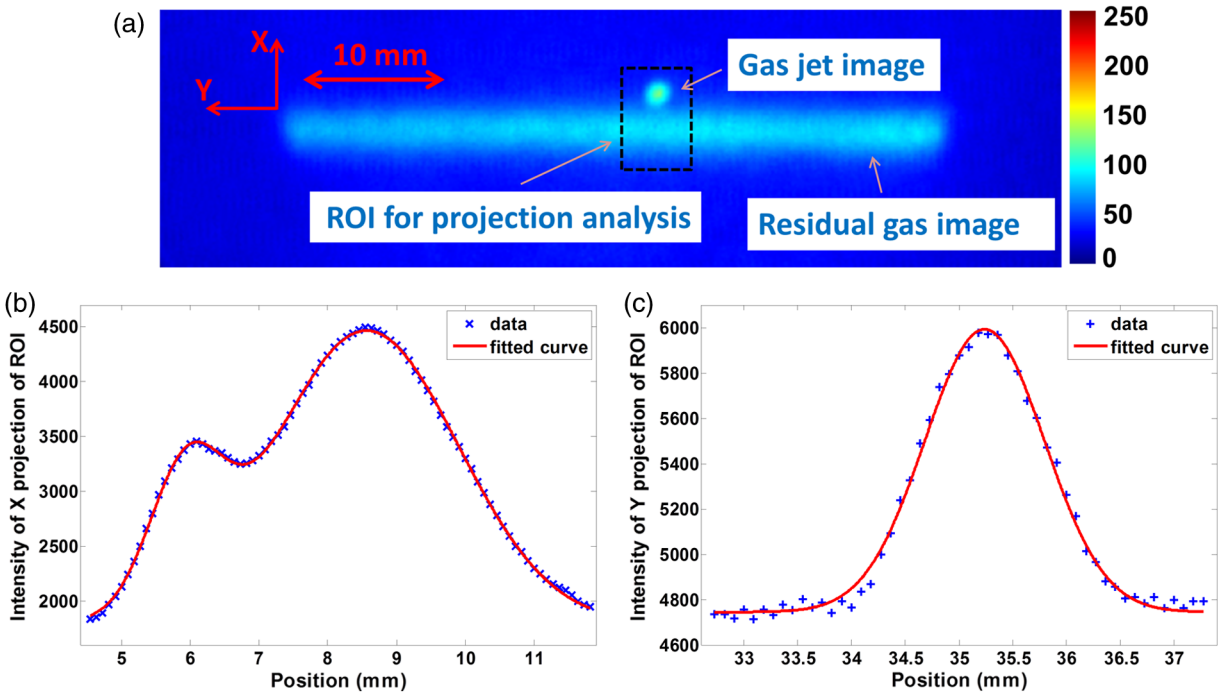

FIG. 17. (a) Images of the electron beam profile from both gas jet and residual gas; projected profiles in (b) x direction and (c) y direction (electron beam energy is 3.5 keV, external collecting E-field is 8.0 kV/m, the gas pulse duration time is 1 s, and the exposure time of the camera is 120 ms in the middle of the pulse).

repeller plate, top metallic ring plate, MCP and phosphor screen were 300, −1300, −2100 and 3000 V, respectively. The corresponding electrostatic gradient between the repeller plate and the bottom ring electrode was about 8.0 kV/m. The resulting image is shown in Fig. 17(a). Compared to Fig. 16, the increased filament current is not sufficient to compensate for the intensity reduction due to the smaller skimmer. The background noise and the intensity of the residual gas image are both increased. In a real beam line application with much lower vacuum pressure, and with no interference from scattered or reflected electrons, this noise will be greatly reduced. It should be noted here that good synchronization between the pulsed valve and a sensitive camera can also improve the image quality, because the intensity of the gas jet-induced signal rises much faster than that of the ionized residual gas.

For this measurement and the new camera position, the phosphor screen on top of the MCP was 825 pixels in diameter. This gives a calibration factor 11.0 pixels/mm. A ROI was again used to analyze the measured profiles, as indicated by the black dashed line in Fig. 17(a). Figures 17(b) and 17(c) show the x projection and y projection of the ROI, and the curves are fitted in the same way as for the larger skimmer case. The fitting results in beam sizes of $\sigma_{x\_\mathrm{jet}} = 0.54 \pm 0.02$ mm, $\sigma_{y\_\mathrm{jet}} = 0.56 \pm 0.03$ mm for the gas jet image and $\sigma_{x\_\mathrm{res}} = 1.34 \pm 0.02$ mm for the residual gas image. Similarly, from Eq. (1) the beam size in the X axis is $\sigma_{x\_\mathrm{real}} = 0.53$ mm.

For the Y axis, taking into account the jet thickness of 0.28 mm and the thermal spread according to Eq. (2), the beam size is $\sigma_{y\_\mathrm{real}} = 0.47$ mm. It is clear that the difference between the $\sigma_{y,\mathrm{real}}$ and the σ_{y_jet} is much reduced, compared with the larger skimmer case. Therefore, the resolution is indeed improved by using a thinner gas jet curtain. Generally, a smaller third skimmer size has less effect on the measurement resolution along the y axis due to the smaller gas jet thickness. The reduction of the jet thickness decreases the reaction rate however, and a longer integration time might then be required. For every application, the skimmer size must be carefully chosen, based on both the acquisition time and the overall resolution requirements. The results of the beam profile estimation for both large and small skimmers are summarized in Table II.

TABLE II. Summary of the beam profile measurements for both large and small skimmers.

Error term	Value
Large skimmer	$(7.2 \times 1.8\ \mathrm{mm}^2)$
σ_{x_real}	0.38 mm
σ_{y_real}	1.03 mm
Small skimmer	$(4 \times 0.4\ \mathrm{mm}^2)$
σ_{x_real}	0.53 mm
σ_{y_real}	0.47 mm

V. CONCLUSIONS

In this paper, the operation of a gas jet based beam profile monitor with different nozzle skimmer configurations has been demonstrated experimentally using the test stand at the Cockcroft Institute, UK. Detailed analysis of the performance of the monitor, resolution, and pulsed mode operation has all been discussed. As the experimental data suggests, the beam profile imaged by the gas jet has a higher intensity than that imaged by residual gas. With the current imaging setup, the resolution of the system is about 200 μm in the X axis and 300 μm in the Y axis. In addition, pulsed mode operation has shown the potential to further enhance the performance of this monitor by improving the signal to noise ratio, while preserving a better vacuum by decreasing the unnecessary gas load.

With a new three-dimensional translation stage installed, equipped with an ionization gauge, we will be able to measure the three-dimensional gas jet density distribution and understand the gas dynamics better. This is essential to resolve the systematic errors due to gas inhomogeneity and the resolution of the monitor. Tests are also being carried out on a novel quasioptical focusing system which would allow the generation of ultrathin jets with a diameter of a few tens of microns [44], as well as on a laser-based velocity meter [45] for jet characterization.

The gas jet monitor has great potential as a noninvasive beam profile measurement system, especially for high-intensity beams such as the CLIC Drive Beam and the European Spallation Source. For these applications, an extra magnetic field can be applied to reduce the distortion caused by space charge from the projectile beam. Further work is ongoing to evaluate the effect of the beam space charge in such situations. On the basis of the monitor presented here, a fluorescence-based monitor is currently being developed in collaboration with CERN and GSI as the key diagnostic for the LHC electron lens [46], which is necessary for the High Luminosity LHC upgrade.

ACKNOWLEDGMENTS

For the development of this monitor many people have offered significant contributions. In particular M. Putignano, K. U. Kühnel, the MPI-K and Daresbury design offices are highly acknowledged. Work supported by the EU under Grants No. 215080, No. 289191 and No. 721559, the HLLHC-UK project, the Helmholtz Association under Contract No. VG-NG-328, and the STFC Cockcroft Institute core grant.

[1] M. Eshraqi *et al.*, The ESS linac, in *Proceedings of the 5th international Particle Accelerator Conference(IPAC14), Dresden, Germany*, (IEEE, Dresden, 2014), p. 3322, THPME043.

[2] C. P. Welsch *et al.*, Ultralow energy storage ring at FLAIR, Hyperfine Interact. **213**, 205 (2012).

[3] V. Chohan, CERN Report No. CERN-2014-002, 2014, http://cds.cern.ch/record/1694484.

[4] T. Giacomini *et al.*, Ionization profile monitors–IPM @ GSI, in *Proceedings of the 10th European Workshop on Beam Diagnostics and Instrumentation for Particle Accelerators, Hamburg, Germany* (DESY, Hamburg, 2011), TUPD51.

[5] J. Mießner, M. Sachwitz, M. Markert, R. Sternberger, K. Tiedtke, and A. Hofmann, An ionization profile monitor for the determination of the FLASH photon beam parameter, Nucl. Instrum. Methods Phys. Res., Sect. A **635**, S104 (2011).

[6] T. Tsang, D. Gassner, and M. Minty, Residual gas fluorescence monitor for relativistic heavy ions at RHIC, Phys. Rev. ST Accel. Beams **16**, 102802 (2013).

[7] D. A. Bartkoski, C. Deibele, and Y. Polsky, Design of an ionization profile monitor for the SNS accumulator ring, Nucl. Instrum. Methods Phys. Res., Sect. A **767**, 379 (2014).

[8] R. Connolly, R. Michnoff, T. Moore, T. Shea, and S. Tepikian, Beam profile measurements and transverse phase-space reconstruction on the relativistic heavy-ion collider, Nucl. Instrum. Methods Phys. Res., Sect. A **443**, 215 (2000).

[9] P. Forck, Minimal invasive beam profile monitors for high intense hadron beams, in *Proceedings of the International Particle Accelerator Conference, Kyoto, Japan* (ICR, Kyoto, 2010), TUZMH01.

[10] F. Becker, C. Andre, F. M. Bieniosek, P. Forck, P. A. Ni, and D. H. H. Hoffmann, Beam induced fluorescence (BIF) monitor for intense heavy ion beams, in *Proceedings of BIW08, Tahoe City, California, USA* (JACoW, Geneva, 2008), p. 236, TUPTPF054.

[11] F. Becker *et al.*, Beam induced fluorescence—Profile monitoring for targets and transport, in *Proceedings of HB2012, Beijing, China, 2012* (JACoW, Geneva, 2012), THO3C03.

[12] M. Putignano, K.-U. Kühnel, C.-D. Schröter, and C. P. Welsch, A fast, low perturbation ionization beam profile monitor based on a gas-jet curtain for the ultralow energy storage ring, Hyperfine Interact. **194**, 189 (2009).

[13] B. Vosicki and K. Zankel, The sodium curtain beam profile monitor of the ISR, IEEE Trans. Nucl. Sci. **22**, 1475 (1975).

[14] A. V.Bubley, V. I. Kudelainen, V. V. Parkhomchuk, B. M. Smirnov, and V. S.Tup, Magnesium jet profile monitor, in *Proceedings of 17th International Conference on High Energy Accelerators, Dubna, Russia* (Joint Inst. Nucl. Res., Dubna, 1998), pp. 357–359.

[15] R. Galiana *et al.*, A carbon jet beam profile monitor for LEAR, in *Proceedings of the 1991 Particle Accelerator Conference, San Francisco, CA, 1991* (IEEE, New York, 1991), pp. 1198–1200.

[16] E. Takada, Carbon ion radiotherapy at NIRS-HIMAC, Nucl. Phys. **A834**, 730c (2010).

[17] Y. Hashimoto, T. Fujisawa, T. Morimoto, Y. Fujita, T. Honma, S. Muto, K. Noda, Y. Sato, and S. Yamada, Oxygen gas-sheet beam profile monitor for the synchrotron and storage ring, Nucl. Instrum. Methods Phys. Res., Sect. A **527**, 289 (2004).

[18] T. Fujisawa, Y. Hashimoto, T. Morimoto, and Y. Fujita, Multipole magnets to focus an O_2 sheet beam for a nondestructive beam-profile monitor, Nucl. Instrum. Methods Phys. Res., Sect. A **506**, 50 (2003).

[19] S. Sawada, J-PARC facility, Nucl. Phys. **A834**, 701c (2010).

[20] Y. Hashimoto, Y. Hori, T. Morimoto, T. Toyama, M. Uota, T. Fujisawa, T. Murakami, K. Noda, D. Ohsawa, Development of a beam profile monitor using nitrogen molecular jet for intense beams, in *Proceedings of 1st International Beam Instrumentation Conference (IBIC2012), Tsukuba, Japan* (JACoW, Geneva, 2013), p. 511, TUPB73.

[21] Y. Hashimoto, Y. Hori, T. Morimoto, S. Muto, T. Toyama, K. Yoshimura, T. Fujisawa, T. Murakami, K. Noda, and D. Ohsawa, Development of a beam profile monitor using a nitrogen-molecular jet for the J-PARC MR, in *Proceedings of 2nd International Beam Instrumentation Conference (IBIC2013), Oxford, UK* (JACoW, Geneva, 2013), p. 848, WEPF17.

[22] T. Tsang, S. Bellavia, R. Connolly, D. Gassner, Y. Makdisi, T. Russo, P. Thieberger, D. Trbojevic, and A. Zelenski, Optical beam profile monitor and residual gas fluorescence at the relativistic heavy ion collider polarized hydrogen jet, Rev. Sci. Instrum. **79**, 105103 (2008).

[23] J. Ullrich, R. Moshammer, A. Dorn, R. D rner, L P. H. Schmidt, and H. Schmidt-B cking, Recoil-ion and electron momentum spectroscopy: reaction-microscopes, Rep. Prog. Phys. **66**, 1463 (2003).

[24] M. Putignano, Ph.D. thesis, University of Liverpool, 2012.

[25] *Atomic and Molecular Beam Methods*, edited by G. Scoles *et al.* (Oxford University Press, New York, 1988), Vol. 1.

[26] MHE3-MS1H-3/2G-1/8 solenoid pulsed valve by Festo, https://www.festo.com/cat/no_no/products_MH2.

[27] TGP110 pulse generator by Aim & Thurlby Thandar Instruments, http://www.aimtti.com/.

[28] dc power supply IPS-3303 by ISO-Tech, http://www.iso-techonline.com/.

[29] Solid state relay DMO063 by Crydom, http://www.crydom.com/en/.

[30] Molecular beam skimmers by Beam Dynamics, Inc., http://www.beamdynamicsinc.com/.

[31] V. Tzoganis, A. Jeff, and C. P. Welsch, Gas dynamics considerations in a noninvasive profile monitor for charged particle beams, Vacuum **109**, 417 (2014).

[32] HV Power Supplies by MicroLab Devices, http://www.microlabdevices.com/.

[33] Microchannel Plates by PHOTONIS, http://www.photonis.com/en/microchannel-plates.

[34] Grasshopper3 2.3 MP camera by Point Gray, https://www.ptgrey.com/grasshopper3-usb3-vision-cameras.

[35] E-Gun ELS 5000 by PSP Vacuum Technology, http://www.pspvacuum.com/electron_source_for_aes.html.

[36] V. Tzoganis and C. P. Welsch, A noninvasive beam profile monitor for charged particle beams, Appl. Phys. Lett. **104**, 204104 (2014).

[37] M. G. Bulmer, *Principles of Statistics* (Dover Publications, New York, 1979).

[38] T. Kirchner and H. Knudsen, Current status of antiproton impact ionization of atoms and molecules: theoretical and experimental perspectives, J. Phys. B **44**, 122001 (2011).

[39] P. L. Bartlett and A. T. Stelbovics, Electron-impact ionization cross sections for elements $Z = 1$ to $Z = 54$, At. Data Nucl. Data Tables **86**, 235 (2004).

[40] H. Zhang, V. Tzoganis, A. Jeff, and C.P. Welsch, Development of a supersonic gas-jet beam profile monitor, in *Proceedings of 4th International Beam Instrumentation Conference (IBIC2015), Melbourne, Australia* (JACoW, Geneva, 2016), p. 530, TUPB075.

[41] A. Friedman, R. H. Cohen, D. P. Grote, S. M. Lund, W. M. Sharp, J.-L. Vay, I. Haber, and R. A. Kishek, Computational methods in the Warp code framework for kinetic simulations of particle beams and plasmas, IEEE Trans. Plasma Sci. **42**, 1321 (2014).

[42] K. Satou *et al.*, A prototype of residual gas ionization profile monitor for J-PARC RCS, in *Proceedings of the 10th European Particle Accelerator Conference, Edinburgh, Scotland, 2006* (EPS-AG, Edinburgh, Scotland, 2006), TUPCH065.

[43] R. Schuch, H. Schöne, P. D. Miller, H. F. Krause, P. F. Dittner, S. Datz, and R. E. Olson, Charge- and Angle-Correlated Inelasticities in Collisions of Bare Fast Carbon Ions with Neon, Phys. Rev. Lett. **60**, 925 (1988).

[44] A. Jeff *et al.*, A quantum gas jet for noninvasive beam profile measurement, in *Proceedings of 3rd International Beam Instrumentation Conference (IBIC2014), Monterey, CA, USA* (JACoW, Geneva, 2016), p. 284, TUCZB3.

[45] A. S. Alexandrova, V. Tzoganis, and C. P. Welsch, Laser diode self-mixing interferometry for velocity measurements, Opt. Eng. (Bellingham, Wash.) **54**, 034104 (2015).

[46] G. Stancari *et al.*, Conceptual design of hollow electron lenses for beam halo control in the Large Hadron Collider, arXiv:1405.2033.